

1 Long-term Determination of Energetic Electron Precipitation into the
2 Atmosphere from AARDDVARK Subionospheric VLF Observations

3 Jason J. Neal and Craig J. Rodger

4 Department of Physics, University of Otago, Dunedin, New Zealand

5 Mark A. Clilverd

6 British Antarctic Survey (NERC), Cambridge, United Kingdom

7 Neil R. Thomson

8 Department of Physics, University of Otago, Dunedin, New Zealand

9 Tero Raita and Thomas Ulich

10 Sodankylä Geophysical Observatory, University of Oulu, Sodankylä, Finland

11 **Abstract.** We analyze observations of subionospherically propagating very low frequency
12 (VLF) radio waves to determine outer radiation belt Energetic Electron Precipitation (EEP)
13 flux magnitudes. The radio wave receiver in Sodankylä, Finland (SGO) observes signals
14 from the transmitter with call sign NAA (Cutler, Maine). The receiver is part of the
15 Antarctic-Arctic Radiation-belt Dynamic Deposition VLF Atmospheric Research Konsortia
16 (AARDDVARK). We use a near-continuous dataset spanning November 2004 until
17 December 2013 to determine the long time period EEP variations. We determine quiet day
18 curves (QDC) over the entire period and use these to identify propagation disturbances
19 caused by EEP. LWPC radio wave propagation modeling is used to estimate the
20 precipitating electron flux magnitudes from the observed amplitude disturbances, allowing
21 for solar cycle changes in the ambient D-region and dynamic variations in the EEP energy
22 spectra. Our method performs well during the summer months when the day-lit ionosphere
23 is the most stable, but fails during the winter. From the summer observations we have
24 obtained 693 days worth of hourly EEP flux magnitudes over the 2004-2013 period. These

25 AARDDVARK-based fluxes agree well with independent satellite precipitation
26 measurements during high intensity events. However, our method of EEP detection is 10-50
27 times more sensitive to low flux levels than the satellite measurements. Our EEP variations
28 also show good agreement with the variation in lowerband chorus wave powers, providing
29 some confidence that chorus is the primary driver for the outer-belt precipitation we are
30 monitoring.

31 **1. Introduction**

32 More than 55 years since the discovery of the radiation belts there are still significant
33 uncertainties about the source, loss, and transport of energetic particles inside the belts
34 [Reeves *et al.*, 2009]. A particle may resonate with different magnetospheric waves, causing
35 simultaneous change in one or more of the particles pitch angle, momentum, or position
36 which cause the outer radiation belt to be highly dynamic [Thorne, 2010], with fluxes of
37 energetic electrons changing by >3 orders of magnitude over time scales of hours to days
38 [Li and Temerin, 2001; Morley *et al.*, 2010]. For about the last 10 years there has been
39 strong focus by the scientific community on the highly dynamic nature of the radiation
40 belts. This has likely been partially stimulated by the development and launch on 30 August
41 2012 of NASA's Van Allen Probes which have the primary scientific goal of understanding
42 the acceleration, transport and loss processes affecting radiation belt particles.

43 It has long been recognized that the magnitude of the flux of trapped electrons in the outer
44 radiation belt is a "delicate balance between acceleration and loss" [Reeves *et al.*, 2003]
45 where significant increases or decreases in the trapped electron flux can occur depending on
46 whether the acceleration or loss processes dominate. Energetic Electron Precipitation (EEP)
47 is one significant loss mechanism for the outer radiation belt [e.g., Thorne *et al.*, 2005;
48 Morley *et al.*, 2010; Hendry *et al.*, 2012; Ni *et al.*, 2013], by which high energy electrons are
49 lost out of the radiation belts through collisions with the atmosphere. Quantifying the

50 magnitudes of precipitating electron flux as well as their spatial and temporal distributions
51 are important for a full understanding of the radiation belt dynamics as they also act as an
52 indicator for the mechanisms occurring inside the belts [Ni *et al.*, 2013]. For example,
53 observations have shown that there are consistently very strong dropouts in the outer belt
54 electron fluxes during the small-moderate geomagnetic disturbances associated with the
55 arrival of a high speed associated solar wind stream interface at the magnetosphere [Morley
56 *et al.*, 2010]. Increasing evidence points to the main driver of these dropouts being
57 magnetopause shadowing [Turner *et al.*, 2013] without a significant contribution from
58 electron precipitation during the dropout [Meredith *et al.*, 2011]. However, immediately
59 following the dropout, as the acceleration processes start to rebuild the trapped fluxes, there
60 are very significant precipitation levels [Hendry *et al.*, 2012] likely due to wave-particle
61 interactions with chorus [Li *et al.*, 2013].

62 There is growing evidence that energetic electron precipitation (EEP) from the radiation
63 belts may play an important role in the chemical makeup of the polar mesosphere,
64 potentially influencing atmospheric dynamics and polar surface climate. It has long been
65 recognized in the radiation belt community that relativistic electron precipitation (REP) can
66 provide a additional source of ozone destroying odd nitrogen [Thorne, 1977], leading that
67 author to conclude that the effects of EEP "must also be considered in future photochemical
68 modeling of the terrestrial ozone layer". There is growing evidence in support of this basic
69 idea, albeit concerning mesospheric ozone rather than affects in the stratospheric ozone
70 layer.

71 Particle precipitation can lead to catalytic ozone destruction due to the reactions with
72 precipitation-produced odd nitrogen and odd hydrogen in the Earth's atmosphere [Brasseur
73 *and Solomon*, 2005]. The first confirmation of this came from experimental observations
74 during solar proton events, where significant ozone destruction occurred in the mesospheric
75 polar atmosphere [e.g., Seppälä *et al.*, 2006; 2007]. In addition there is growing evidence of

76 high levels of energetic electron precipitation (EEP) during both geomagnetic storms and
77 substorms [e.g., *Rodger et al.*, 2007a; *Cliiverd et al.*, 2012]. The EEP intensities in these
78 examples are sufficient to produce significant polar region mesospheric chemical changes
79 [*Rodger et al.*, 2010b], of similar magnitude to a medium sized solar proton event.
80 Mesospheric observation of the EEP chemical changes have now been reported caused by
81 the direct effect of the precipitation [e.g., odd nitrogen: *Newnham et al.*, 2011; odd
82 hydrogen: *Verronen et al.*, 2011; *Andersson et al.*, 2012, 2013] with subsequent ozone
83 decreases [*Daae et al.*, 2012; *Andersson et al.*, 2014a]. Detectable EEP-produced odd
84 hydrogen increases have been reported due to electrons from ~100 keV to ~3 MeV, leading
85 to increases from ~82 km to 52 km altitude [*Andersson et al.*, 2012]. Superposed epoch
86 analysis of mesospheric ozone decreases at 70-80 km immediately after EEP events from
87 2004-2009 indicated the magnitudes of these short-term depletions are comparable to those
88 caused by larger but much less frequent solar proton events [*Andersson et al.*, 2014b].

89 There is evidence that EEP may influence polar surface climate. Large (± 2 K) variations in
90 polar surface air temperatures have been produced in chemistry-climate models after NO_x
91 sources were imposed to represent the atmospheric impact of EEP [*Rozanov et al.*, 2005;
92 *Baumgaertner et al.*, 2011]. These modeling studies have been tested using experimentally
93 derived operational surface level air temperature data sets (ERA-40 and ECMWF),
94 examining how polar temperatures vary with geomagnetic activity [*Seppälä et al.*, 2009].
95 This test produced similar patterns in surface level air temperature variability as the
96 modeling studies, but with temperatures differing by as much as ± 4.5 K between high and
97 low geomagnetic storm periods. It was also found that changing solar irradiance/EUV-
98 levels did not drive the observed surface level air temperature variability. *Seppälä et al.*
99 [2009] argued that the primary reason for the temperature variability was mostly likely EEP
100 causing ozone decreases through NO_x production. More recently ERA-40 re-analysis data
101 has been examined to see how the EEP-produced atmospheric changes might couple to

102 stratospheric dynamics [*Seppälä et al.*, 2013], concluding that that EEP-generated NO_x
103 altered planetary wave breaking in the lower stratosphere. The change in the locations of
104 planetary wave breaking allows more planetary waves to propagate into the upper
105 stratosphere in low latitudes, leading to the observed dynamical responses.

106 Further studies making use of chemistry climate models require realistic EEP observations.
107 This has led to increased focus on EEP- measurements, as well efforts to incorporate such
108 particle inputs into climate models through the development of systems such as the
109 Atmospheric Ionization Module OSnabrück (AIMOS) model [*Wissing et al.*, 2009].
110 AIMOS combines experimental observations from low-Earth orbiting and geostationary
111 orbiting spacecraft with geomagnetic observations to provide a 3-D numerical model of
112 atmospheric ionization due to precipitating particles.

113 One of the most commonly used source of EEP measurements is the Medium Energy
114 Proton and Electron Detector (MEPED) instrument in the Space Environment Monitor-2
115 (SEM-2) experimental package onboard the Polar-orbiting Operational Environmental
116 Satellites (POES) spacecraft, which is described in more detail below. However, there are
117 numerous concerns and issues surrounding these experimental measurements, including
118 contamination by low-energy protons [e.g., *Rodger et al.*, 2010a; *Yando et al.*, 2011], over-
119 whelming contamination in solar proton events as well as inner radiation belt protons in the
120 SAMA [*Rodger et al.*, 2013], and the size of the pitch angle range sampled by the telescope
121 relative to the bounce loss cone size [*Hargreaves et al.*, 2010; *Rodger et al.*, 2013].

122 In this paper we use ground-based subionospheric Very Low Frequency (VLF)
123 observations to determine EEP fluxes during the northern hemisphere summer months
124 spanning 2005-2013. We undertake comparisons with the POES EEP measurements, as
125 well as the whistler mode chorus intensities which may be driving the precipitation through
126 wave-particle interactions. Our study builds on an earlier ground-based paper by *Cilverd et*
127 *al.* [2010] by using: a larger dataset (November 2004-December 2013), a more sophisticated

128 analysis of the subionospheric data, as well as multiple improvements to the modeling
129 approach, including allowing for changing energy spectral gradients in the EEP and solar-
130 cycle changes in the ambient D-region ionosphere. We also present some data quality
131 checks undertaken on the AIMOS model output. We attempt to validate the model with our
132 improving understanding of EEP from the MEPED/POES and AARDDVARK
133 observations. This is the first attempt to validate AIMOS model outputs for electron
134 energies greater than ~ 10 keV, which is necessary as the model is now being used to
135 examine mesospheric EEP impacts by some authors [e.g., *Funke et al.*, 2011].

136 **2. Experimental Setup**

137 **2.1 AARDVARK Observations**

138 Antarctic-Arctic Radiation-belt Dynamic Deposition VLF Atmospheric Research
139 Konsortia (AARDDVARK) is a global network of radio wave receivers which monitor
140 powerful narrow-band VLF (very low frequency) transmitters. Subionospherically
141 propagating VLF waves are used to monitor Energetic Electron Precipitation (EEP) through
142 changes in the ionization rates of the lower ionosphere (50-90 km). Excess ionization
143 caused by EEP causes perturbations in the amplitude and phase of received VLF signals,
144 which can found through comparison with the quiet day propagation levels. Radio wave
145 propagation modeling may then be used to determine the EEP fluxes required to cause the
146 observed changes, following the techniques outlined in *Rodger et al.* [2012].

147 We primarily focus on the radio wave observations made by the two AARDDVARK
148 receivers situated at Sodankylä (SGO), Finland ($67^{\circ}13'N$, $26^{\circ}22'E$, $L = 5.2$). These were an
149 OmniPAL receiver (operational November 2004 – April 2013 [*Dowden et al.*, 1998]) and
150 the newer UltraMSK receiver (operational April 2010 – present; [*Clilverd et al.*, 2009]).
151 Both receivers monitor the minimum-shift keying (MSK) VLF transmissions from a
152 communications station located in Cutler, Maine, USA (24.0 kHz, $44^{\circ}35'N$, $67^{\circ}16'W$, $L =$

153 2.9), which has the call sign NAA. The transatlantic path between NAA and SGO lies
154 directly underneath the outer radiation belt ($L = 3-7$) such that the VLF transmissions along
155 this path are directly influenced by outer radiation belt energetic electron precipitation. The
156 left hand panel of Figure 1 presents a map showing the transmitter and receiver locations as
157 well as the propagation great circle path. Lines of constant L are displayed to indicate the
158 footprints of the outer radiation belt. The monthly averaged A_p values and sunspot number
159 are displayed in the right hand panels of Figure 1, showing the entire time period
160 considered. This gives an indication of the changing conditions across the ~9 year Nov
161 2004- Dec 2013 period, which spans most of a solar cycle.

162 AARDDVARK NAA median amplitude measurements at SGO with 1 minute time
163 resolution were constructed from the 0.2 s native resolution data. The measurements from
164 the two independent receivers were combined together to provide a more continuous
165 dataset. By comparing the observations across the 3 years when the two receivers were
166 operating simultaneously we have been able to successfully combine the datasets, with the
167 UltraMSK eventually replacing the OmniPAL after it suffered a terminal failure in mid-
168 2013. This combination leads to our very long (>9 year) dataset of 1 minute resolution
169 NAA-SGO amplitude measurements. A careful check was undertaken to remove any
170 erroneous data associated with receiver or transmitter operational problems, and correcting
171 for some timing discrepancies. Figure 2 shows the 2859 days of NAA-SGO median
172 amplitude observations after these checks (~327 days of erroneous OmniPAL data were
173 removed and ~143 days of erroneous UltraMSK data). Distinct patterns are clearly visible
174 in the amplitude data corresponding to seasonal and daily variation in the ionosphere,
175 mostly due to the changing solar zenith angles. One of the main features present in the data
176 is the effect of sunrise (~8 UT) and sunset (~20 UT) on the path and the seasonal variation
177 affecting the length of the sunlit period across the path. A deep minimum can be seen in the
178 midday amplitude data during winter time in 2009-2010, corresponding to the period of

179 solar minimum. This demonstrates the expected dependence of the ionospheric D-region
180 (and hence subionospheric propagation) on the changing solar cycle [*Thomson and Clilverd,*
181 2000].

182 The NAA-SGO subionospheric VLF path is affected by the impact of solar proton events
183 on the D-region along that path [*Rodger et al., 2006, 2007a*]. Any attempt to monitor EEP
184 using NAA-SGO subionospheric observations will potentially be confounded by the strong
185 ionospheric response to solar protons; hence we remove 144.8 days worth of 1-minute
186 amplitude observations from our analysis, leaving a total of 2714.6 days worth of
187 observations remaining. Solar proton events were identified using the list provided by
188 NOAA (available at <http://www.swpc.noaa.gov/ftplib/indices/SPE.txt>) which provides the
189 >10 MeV proton flux observed at geostationary orbit over the time period 1976-present.
190 Note that a solar proton event in this list is defined as spanning the time from when the flux
191 climbs above 10 pfu (where pfu is the proton flux unit [$\text{protons}\cdot\text{s}^{-1}\text{sr}^{-1}\text{cm}^{-2}$ for >10 MeV
192 protons measured at geostationary orbit]) to when the flux again falls below this value.

193

194 **2.2 POES EEP Observations**

195 The Polar Orbiting Environmental Satellites (POES) are low altitude (~800-850 km)
196 spacecraft with Sun-synchronous polar orbits with periods of ~100 minutes. Since 1998 the
197 POES spacecraft have carried the second generation SEM-2 [*Evans and Greer, 2004*] which
198 measures energetic charged-particle fluxes using the Medium Energy Proton and Electron
199 Detector. To date 7 POES spacecraft have operated the SEM-2 package in orbit (NOAA 15-
200 19 and also MetOp 1-2). The SEM-2 detectors include integral electron telescopes with
201 energies of >30 keV (e1), >100 keV (e2), and >300 keV (e3), pointed in two directions. In
202 this study we focus primarily upon the 0°-pointing detectors, as this primarily monitors deep
203 inside the Bounce Loss Cone (BLC) [*Rodger et al., Appendix A, 2010a*]. Previous studies
204 have identified significant contamination in the electron channels by protons with energies

205 of hundreds of keV [*Yando et al.*, 2011], which are particularly significant during storm
206 times. We correct this using a NOAA-developed algorithm as described in Appendix A of
207 *Lam et al.* [2010], and recently validated by *Whittaker et al.* [2014]. We follow *Rodger et*
208 *al.* [2013] and remove these periods using the MEPED P7 omni-directional observations of
209 >36 MeV protons. We first combine the POES-reported particle fluxes varying with IGRF L
210 and time, using 0.25- L and 15-min time resolution. Observations from inside and around the
211 South Atlantic Magnetic Anomaly are excluded before the measurements are combined,
212 although the P7 test to exclude solar proton events also suppresses all measurements in the
213 SAMA-region, where inner radiation belt protons swamp the electron detectors [*Rodger et*
214 *al.*, 2013]. The variation of the hourly outer belt >30 keV EEP fluxes is shown in the left
215 hand panel of Figure 3. Note that in 2009 the POES EEP drops to very low precipitation
216 levels (noise-floor level). This time period spans an extended period of low solar activity, in
217 which the trapped LEO relativistic electron fluxes reported by SAMPEX [*Russell et al.*,
218 2010] and the geosynchronous GOES observations both fell to noise floor levels. Similar
219 decreases in the POES trapped relativistic electrons have been reported, which were noted
220 as being "unprecedented in the ~ 14 years of SEM-2 observations" [*Cresswell-Moorcock et*
221 *al.*, 2013]. In the same time period that study noted the outer belt >100 keV POES trapped
222 electron fluxes decreased by 1-1.5 orders of magnitude, recovering to the typical long term
223 average in 2010.

224 We fit a powerlaw spectrum to the three 0° electron telescopes to obtain the energy
225 spectral gradient (k) for the precipitating electrons; a recent comparison between the high
226 energy resolution DEMETER electron flux observations with POES has reported power-
227 laws were accurate representations of the flux spectrum [*Whittaker et al.*, 2013]. The
228 resulting POES spectra are used in the modeling sections of the current study to help
229 determine the EEP fluxes from the NAA-SGO AARDDVARK observations. The
230 MEPED/POES >30 keV BLC fluxes will be later contrasted with the EEP fluxes reported

231 from the AARDDVARK amplitude differences. At the same time >100 keV (e2) and
232 >300 keV (e3) EEP will also be taking place and reported by POES. However, we use the
233 >30 keV (e1) for our comparisons as these fluxes are consistently larger, and thus more
234 likely to be above the MEPED/POES noise floor levels. Note that there is a strong
235 correlation between the fluxes in e1, e2 and e3 (as discussed in section 5.2).

236 **2.3 DEMETER Lower-Band Chorus**

237 As well as comparing the NAA-SGO EEP fluxes to the POES EEP measurements we also
238 investigate the connection to likely plasma wave drivers causing the EEP. We make use of
239 observations from the ICE (Instrument Champ Electrique) instrument onboard the
240 DEMETER spacecraft to examine this. The DEMETER satellite was launched in June 2004,
241 flying at an altitude of 670 km (after 2005) in a Sun-synchronous orbit with an inclination
242 of 98° . The ICE instrument provides continuous measurements of the power spectrum of
243 one electric field component in the VLF band [Berthelier *et al.*, 2006]. Here we make use of
244 both survey and burst mode data of the electric field spectra recorded up to 20 kHz, with a
245 frequency channel resolution of 19.25 Hz. We analyze ICE/DEMETER data up to early
246 December 2010, shortly before the deorbiting of the satellite in March 2011. The high-time
247 resolution ICE/DEMETER data has been re-processed to determine the hourly mean
248 intensity of waves over $L = 3-7$ in the frequency band from $0.1-0.5 f_{ce}$, where lower band
249 chorus occurs. We combine both the "day" and "night" DEMETER observations, i.e., there
250 is no restriction on MLT, to produce the highest possible time resolution. Note that
251 DEMETER has previously been used to study whistler-mode chorus, despite its
252 comparatively low altitude [e.g., Santolik *et al.*, 2006, Zhima *et al.*, 2013]. The right hand
253 panel of Figure 3 shows the variation in the observed median DEMETER lower-band
254 chorus wave power across the entire mission life. Once again the solar minimum period in
255 2009 shows lower levels of chorus intensity, emphasizing the quietness of this time.

256 **3. QDC Generation**

257 The Quiet Day Curve (QDC) describes the annual and daily background (which one might
258 also term, "quiet" or "undisturbed") variation in the received VLF amplitude measurements.
259 The received amplitudes of fixed frequency VLF transmissions vary in a constant manner
260 during undisturbed conditions. Energetic Electron Precipitation (EEP) events can be detected
261 as deviations from the subionospheric quiet day curve as a change in amplitude of the
262 received signal relative to the QDC [Rodger *et al.*, 2012; Simon Wedlund *et al.*, 2014]. This is
263 equivalent to the QDC approach used for riometers which has become standard practice in
264 that community.

265 For the NAA-SGO path EEP causes changes in the D-region electron density which tend to
266 lead to increases in the received amplitudes, such that the lowest amplitudes occur during the
267 quietest times. This is most reliable for time periods when the NAA-SGO path is dominated
268 by a Sun-lit ionosphere. The consistent amplitude increases during summertime D-region
269 perturbation times was identified by *Clilverd et al.* [2010], who exploited it to manually
270 produce QDCs for 3 different UT time slices 2-3, 8-9, and 16-17 UT to determine the EEP
271 magnitudes. In our study we have also exploited the same behavior, but developed an
272 automatic process to produce QDCs for all UT times directly from the observed
273 subionospheric VLF amplitudes. For each UT hour we determine the mean and standard
274 deviation of the experimentally observed amplitude values. The QDC was generated by
275 subtracting two standard deviations from the mean and then smoothed with a 19-day sliding
276 average. We investigated a range of possible averaging windows, from 3-51 days, and
277 concluded that 19 days performed the best, giving a smoothly varying QDC without rounding
278 away the large modal features present. The left hand panel of Figure 4 shows the QDCs
279 determined for 2-3, 8-9, and 16-17 UT for the 2005 observations, along with the QDCs for
280 the same 1 hour time periods from *Clilverd et al.* [2010]. Our approach leads to a QDC that
281 follows the lower edge of the amplitude data (blue line) and has similar shape to that given by

282 *Clilverd et al.* [2010] for the 2005 QDCs (red line) determined from their somewhat naïve
283 "straight line" minimum approach.

284 The right hand panel of Figure 4 shows the QDC generated at 1-hour time resolution across
285 the entire ~9 year period of experimental observations. A deep midday minimum can be seen
286 in 2009/2010 during the winter, i.e., during the solar minimum. However, the opposite
287 behavior can be seen for the noon-time summer amplitudes; the QDC amplitude for solar
288 minimum (2009/2010) is ~2.3 dB higher than seen during solar maximum in 2005. This is
289 addressed further in Section 4.1.

290 **4. Modeling of EEP Impact on VLF propagation**

291 In order to interpret the significance of observed changes in a received VLF signal it is
292 necessary to make use of a propagation model. This allows one to link the properties of the
293 ionization changes occurring around the upper boundary of the Earth ionosphere waveguide
294 (i.e., the lower part of the D-region) with the magnitude of the changes in the VLF
295 transmissions. Here we use the US Navy Long Wave Propagation Code [LWPC, *Ferguson*
296 *and Snyder*, 1990]. LWPC models the propagation of fixed-frequency VLF waves from a
297 transmitter to a receiver, calculating the received amplitude and phase. The great circle path
298 between these two points is broken into a series of segments, accounting for changes in
299 geophysical parameters along the path to be allowed for. For each segment the programme
300 takes into account variations in: ground conductivity, dielectric constant, orientation of the
301 geomagnetic field with respect to the path, solar zenith angle and also the electron density
302 profile (i.e., electrons m⁻³).

303 The electron density profile is varied by forcing the atmosphere with EEP from above. A
304 short description of the modeling process is given below; for a full description see *Rodger*
305 *et al.* [2012]. A series of coupled models are used to determine the equilibrium electron
306 number density which will subsequently be fed into LWPC: the ionization rates due to the

307 EEP [Rees, 1989; Goldberg *et al.*, 1984], the background neutral atmosphere [Picone *et al.*,
308 2002], and the equilibrium electron number density in the lower ionosphere [Rodger *et al.*,
309 1998, 2007a, 2012]. The electron density profiles are determined for a range of precipitation
310 flux magnitudes and power-law energy spectral gradients ranging from +0.5 to -5 with 0.5
311 steps. We assume the EEP spans the energy range 10 keV to 3 MeV, but report the >30keV
312 flux magnitudes to allow direct comparison with the POES observations. The electron
313 density profiles are then used as inputs into the LWPC subionospheric propagation model,
314 applied uniformly along the path. Thus we model the effect of electron precipitation on the
315 VLF amplitudes from NAA received at Sodankylä.

316 **4.1 Incorporating the D-region Yearly Variability**

317 For undisturbed time periods, the D-region electron density altitude profile is often
318 expressed through a Wait ionosphere, defined in terms of a sharpness parameter β and a
319 reference height H' [Wait and Spies, 1964], with the electron number density increasing
320 exponentially with altitude. The Clilverd *et al.* [2010] study of the NAA-SGO path used
321 fixed ambient daytime ionosphere parameters ($\beta=0.3 \text{ km}^{-1}$, $H'=74 \text{ km}$) consistent with the
322 nondisturbed amplitudes of NAA experimentally observed at SGO for 2005. As seen in
323 Figure 4 there is evidence of changes in the nondisturbed D-region across the solar cycle.
324 We took the mean day-time summer (May-July) amplitude difference for each year and
325 compared those values to that determined from 2005. We observed that the differences in
326 QDC noontime (16-17 UT) amplitudes gradually increase from the relatively high solar
327 activity in 2005 to solar minimum (2009/2010). These changes can be seen in the right hand
328 panel of Figure 4 and also in Figure 5. The maximum variation is $\sim 2.5 \text{ dB}$, after which the
329 amplitude difference decreases as the solar cycle advances towards solar maximum
330 conditions. These changing QDC noontime (16-17 UT) amplitude values were used to
331 determine the variation in the Wait ionospheric β parameter required to represent the solar
332 cycle variations in the D-region from 2005-2013. This was undertaken using LWPC with

333 "quiet" (i.e., zero EEP) propagation modeling. We follow *Clilverd et al.* [2010] and use a β
 334 value of 0.3 km^{-1} for 2005, which increases to produce the observed increasing QDC
 335 amplitudes (Figure 4), such that for solar minimum conditions β has evolved to $\sim 0.42 \text{ km}^{-1}$
 336 (Figure 5). Note the smooth and consistent variation in β shown in Figure 5 with the
 337 progression of the solar cycle. H' was held constant here throughout the solar cycle partly
 338 because *McRae and Thomson* [2000] reported that H' changed by only $\sim 1 \text{ km}$ from solar
 339 maximum to solar minimum at mid-latitudes (no appropriate high-latitude measurements
 340 are available to the best of our knowledge), and partly because LWPC modeling (not
 341 shown) indicates that the amplitude for the NAA-SGO path was only weakly dependent
 342 upon H' . This adjusted beta value is then used in LWPC to produce separate modeling of
 343 the expected impact of EEP on the NAA-SGO amplitudes for each year.

344 **4.2 Incorporating EEP Energy Spectra Variability**

345 The energy spectra of precipitating energetic electrons is well represented by a power law
 346 [*Whittaker et al.*, 2013]. The previous study into EEP monitored using observations from the
 347 NAA-SGO path by *Clilverd et al.* [2010] used modeling based on a fixed power law with a
 348 gradient of $k = -2$. We remove this limitation by using a variable energy spectrum in our
 349 modeling of how the EEP impacts the ionosphere and modified the VLF propagation. The
 350 energy spectral gradient of the precipitating fluxes was varied from $k=-5$ to 0.5 in steps of 0.5 .
 351 The differing spectral gradients lead to significantly different amplitude changes for a given
 352 EEP flux magnitude and ambient ionospheric profile. Examples of this are shown in Figure 6,
 353 which presents the LWPC-predicted amplitudes for a range of EEP magnitudes and spectral
 354 gradients for 2006 (left hand panel) and 2010 (right hand panel).

355 Recently the EEP powerlaw spectral gradient was determined directly from AARDDVARK
 356 measurements made in Canada during a series of geomagnetic storms [*Simon Wedlund et al.*,
 357 2014]. This relied upon simultaneous amplitude perturbation observations on two different
 358 AARDDVARK paths which are likely to sense similar EEP activity, along with LWPC

359 modeling using a range of spectral gradients which were combined to determine the most
360 likely EEP energy spectral gradients occurring for any given time and day. We are unable to
361 apply this approach in the current study, as we do not have an appropriate second path.
362 However, the *Simon Wedlund et al.* [2014] study found good agreement between the POES
363 and AARDDVARK-determined gradients, giving us additional confidence in the use of the
364 POES-fitted energy gradients as we describe in the following section.

365 **5. AARDDVARK-extracted EEP**

366 We now combine the AARDDVARK experimentally observed NAA-SGO amplitudes with
367 the LWPC modeling described above to extract EEP flux magnitudes from the VLF
368 perturbations. The 1-min observations are averaged to produce hourly mean NAA-SGO
369 amplitude leading to 2762.1 days worth of hourly values – note that the ~1.7% increase in the
370 days worth of data is caused by the averaging of partial hours worth of 1-min data being
371 combined to produce the hourly average. The amplitude QDC seen in the right panel of
372 Figure 4 are subtracted from the hourly average amplitude values to produce 2762.1 days
373 worth of amplitude perturbations.

374 In order to use the LWPC modeling results (e.g., Figure 6), an appropriate EEP power law
375 value is required. We use 1-hour resolution POES satellite data to fit a power law to the three
376 EEP electron flux energy ranges and thus produce a dynamic energy spectral gradient for the
377 precipitating electron population. The change in amplitude results produced by the LWPC
378 modeling for the specific power law value are then linearly interpolated to produce the
379 variation in amplitude perturbations with $\log_{10}(\text{flux magnitude})$ for a specific power law
380 gradient. An EEP flux magnitude may be obtained by matching the observed NAA-SGO
381 amplitude with the modeled amplitude, the latter of which may correspond to one or more
382 EEP values. In situations where more than one solution exists the EEP magnitude closest to
383 the previous hour's value is selected. Observed amplitude values larger than the maximum

384 modeled values are excluded. This affects ~108.4 days worth of perturbations, of which only
385 ~1.5 days worth fall in the summer months.

386 At this point our modeling and QDC determination approaches are only reliable when the
387 NAA-SGO path is dominated by solar photo-ionization, i.e., the summer period. *Clilverd et*
388 *al.* [2010] suggested that the approach worked for the middle ~150 days of the year, roughly
389 from 10 April to early September. In the current study we take a more conservative view, and
390 restrict ourselves to observations occurring each year in the 92 day "summer" period from 1
391 May to 1 August. This produces 693.25 days worth of 1-hour resolution EEP values which
392 appear well behaved. Examples of the AARDDVARK-extracted EEP are seen in Figure 7
393 (black lines).

394 **5.1 Comparison with POES-EEP**

395 To check the validity of our EEP flux-extraction process we compare the AARDDVARK-
396 reported fluxes with the >30 keV EEP measurements made by the POES spacecraft. Figure 7
397 shows the variation of the AARDDVARK-extracted EEP fluxes (black lines) for the northern
398 hemisphere summer periods during 2005-2009. The corresponding >30 keV POES EEP
399 observations are shown in Figure 7 by the red line. The AARDDVARK-extracted EEP fluxes
400 are almost independent of the POES measurements, other than the inclusion of the POES-
401 reported power law gradients. Despite being largely independent EEP measures, both datasets
402 show that the EEP in the years closer to solar maximum (2005-2006) were considerably more
403 active than those near solar minimum (2009), which was very quiet. As mentioned above,
404 during solar proton events our ability to detect EEP is masked. In both mid and late July 2005
405 solar proton events occurred, and as such there is no AARDDVARK-extracted EEP for that
406 time period in the upper panel of Figure 7.

407 Figure 7 demonstrates that during large precipitation events both the AARDDVARK and
408 POES EEP fluxes report similar maximum magnitudes. It has been argued previously that the
409 MEPED/POES BLC fluxes may be under-reported for weak precipitation events [*Hargreaves*

410 *et al.*, 2010; *Rodger et al.*, 2013], where the loss cone is not filled. In contrast during strong
 411 EEP events, likely associated with strong diffusion [*Rodger et al.*, 2013; *Clilverd et al.*,
 412 2014], the MEPED/POES BLC fluxes are expected to be more accurate representations of the
 413 precipitating striking the atmosphere, as such one would hope for good agreement between
 414 the AARDDVARK and MEPED/POES fluxes at these times, as seen in Figure 7. The small
 415 size of the MEPED/POES telescopes detector translates into rather low sensitivity at smaller
 416 flux magnitudes [*Yando et al.*, 2011], reflected by their noise floor level of $\sim 150 \text{ el. cm}^{-2} \text{ s}^{-1}$
 417 sr^{-1} (left hand panel of Figure 3). This is also seen in Figure 7, where the MEPED/POES
 418 $>30 \text{ keV}$ EEP flux during quiet periods is constantly $\sim 10^2 \text{ el. cm}^{-2} \text{ s}^{-1} \text{ sr}^{-1}$. The AARDDVARK-
 419 extracted fluxes have a noise floor value which 10-50 times lower than the MEPED/POES
 420 instrument, emphasizing that the true flux into the atmosphere during quiet periods is much
 421 lower than suggested from the satellite observations. This is particularly clear in the 2009
 422 panel of Figure 7, where low-intensity EEP fluxes occur in the AARDDVARK-extracted data
 423 but are poorly represented in the MEPED/POES fluxes.

424 5.2 Estimation of Uncertainties

425 We have also tested the sensitivity of our AARDDVARK-extracted EEP magnitudes to
 426 uncertainties in the AARDDVARK amplitudes. Uncertainties in subionospheric VLF QDC
 427 will depend upon the time of day, the receiver design and the background noise levels. We
 428 follow an earlier study which concluded there was a $\pm 0.3 \text{ dB}$ amplitude uncertainty as a result
 429 of removing the subionospheric QDC at noon time [*Rodger et al.*, 2007a]. The EEP extraction
 430 process described above is rerun for amplitude differences which are 0.3 dB higher and lower
 431 than the observed amplitude perturbation in order to test the sensitivity. As one might expect,
 432 during quiet times the uncertainty levels in the $>30 \text{ keV}$ flux levels are low ($\sim 1\text{-}2 \text{ el. cm}^{-2} \text{ s}^{-1} \text{ sr}^{-1}$)
 433 ¹), but during high EEP periods the uncertainty levels in the $>30 \text{ keV}$ flux levels are
 434 considerably larger ($\sim 10^4 \text{ el. cm}^{-2} \text{ s}^{-1} \text{ sr}^{-1}$). When comparing these values with the observed
 435 EEP flux magnitudes, we find that the uncertainty varies from $\sim 10\text{-}1000\%$, and are typically

436 ~20%. However, this is dominated by the quiet (low flux) periods. During high EEP periods
437 the uncertainties introduced by the amplitude error is a few times larger (i.e., 200-500%).

438 We have also tested the sensitivity of our AARDDVARK-extracted EEP magnitudes to
439 uncertainties in the POES-fitted energy spectral gradients. We assumed that the e1, e2, and e3
440 MEPED/POES EEP flux values had an uncertainty of 50%. We changed the 2005 fluxes by a
441 random amount up to this uncertainty level, but also required that the modified flux in e1 was
442 greater than or equal to that for e2, and that the modified e2 flux was greater than or equal to
443 that for e3. We then undertook the spectral fitting as outlined in section 2.2. This was
444 repeated twenty times, to produce an estimate of the error in the spectral gradients. While our
445 choice of 50% for the error value is fairly arbitrary, it is similar to the ~30% uncertainty
446 estimated as the possible error in the earlier SEM-1 electron flux estimates [*Tan et al.*, 2007].
447 The average uncertainty in the k value was 0.51. We then repeated the process of determining
448 the EEP magnitudes from AARDDVARK-data using the k values modified by the
449 uncertainties found for each one hour period. The average change in magnitude is ~1.8. The
450 EEP flux magnitude changes are not particularly large, with the effect being less significant
451 than allowing k to vary (as discussed in section 7.1).

452 An important assumption in our approach is to assume that the energy spectra of the EEP is
453 well represented by power-law spanning medium and relativistic energies. There is a high
454 correlation between the three electron energy channels reported by the POES spacecraft. The
455 MEPED/POES EEP fluxes described in section 2.2 are strongly correlated with one another.
456 After removing solar proton events and data gaps we find that the correlation of the
457 $\log_{10}(\text{flux})$ of the e1 and e2 channels across our L -shell range is 0.99, for e2 and e3 this value
458 is 0.987, and for e1 and e3 the correlation value is 0.970, although these high-correlation
459 values will be strongly influenced by the noise-floor. As noted in section 2.2, we take some
460 confidence in the use of the power law to describe the energy spectra of the EEP from the
461 high-energy resolution of the DEMETER satellite. This spacecraft primarily measured in the

462 drift loss cone, and hence for pitch angles only slightly above the BLC. The recent *Whitaker*
463 *et al.* [2013, 2014] studies found that the drift loss cone observations by DEMETER, and also
464 the POES telescopes, were best fitted by a power-law. This held for energies spanning
465 medium and relativistic energies (up to ~ 1.2 MeV). Whistler-mode waves, such as chorus,
466 can pitch angle scatter electrons into the BLC over a very wide energy range. For example,
467 recent simulations of chorus driven precipitation reported electrons spanning a few keV to
468 several MeV [*Saito et al.*, 2012], with a lower limit of ~ 10 keV for $L=5$.

469 We note that there is evidence that power laws may not best represent the EEP energy
470 spectrum for relativistic energies. SAMPEX observations of drift loss cone and bounce loss
471 cone relativistic electron (0.5-5.66 MeV) precipitation seem to have been well represented by
472 an exponential dependence [*Tu et al.*, 2010]. The Taranis mission [*Pincon et al.*, 2011] will
473 provide DEMETER-like high energy resolution electron flux measurements for both the drift
474 loss cone and BLC, and may be able to clarify this issue.

475 **5.3 Comparison with DEMETER Chorus Waves**

476 Lower band chorus waves are known to drive electron precipitation via resonant interactions
477 [*Lorentzen et al.*, 2001; *Horne et al.*, 2003], where the rate of precipitation scales in direct
478 proportion to the power spectral intensity of resonant waves [*Millan and Thorne*, 2007]. To
479 test this we have contrasted the lower band chorus wave intensity detected by DEMETER
480 (right hand panel of Figure 3) with our AARDDVARK-extracted EEP fluxes. Figure 8 shows
481 the NAA-SGO >30 keV EEP fluxes (black line) and the DEMETER lower band chorus
482 intensity (blue line) for 2005, 2006 and 2009. In both cases the EEP flux and chorus
483 intensities are medians limited to 2-8 UT (corresponding to ~ 22 -12 MLT along the great
484 circle path) for which dawn chorus activity should be present.

485 This figure indicates that there is a reasonable correlation "by eye" between the EEP flux
486 and the DEMETER chorus intensity, even during the very quiet 2009 period. After removing
487 solar proton events and data gaps we find that the correlation of the between the EEP flux and

488 the DEMETER chorus intensity is 0.33, which is a modest-moderate level of correlation. It is
489 often assumed that whistler mode chorus waves are the dominant cause of energetic electron
490 precipitation outside of the plasmopause. Our observations provide some support for this
491 assumption, which is backed by published theory and also wave observations. Recently
492 MEPED/POES >30 keV EEP observations were successfully used to predict chorus
493 occurrence, validated by observations from the Van Allan Probes [*Li et al.*, 2013]. This
494 approach is now being used to infer the chorus wave intensity and construct its global
495 distribution directly from POES-observations [*Ni et al.*, 2014], rather than relying on
496 statistical models of wave occurrence.

497 **6. Examination of the AIMOS model**

498 As part of the Quantifying Hemispheric Differences in Particle Forcing Effects on
499 Stratospheric Ozone international team project hosted by the Swiss International Space
500 Science Institute, an attempt was made to validate the precipitation-driven ionization rates
501 reported by the AIMOS model [*Wissing et al.*, 2009]. AIMOS combines particle observations
502 from low-Earth POES and also geostationary orbiting spacecraft with geomagnetic
503 observations to provide 3-D numerical model of atmospheric ionization due to precipitating
504 particles with high spatial resolution. Part of the validation effort involves comparison with
505 ground-based radio wave observations the initial stages of which have been reported
506 elsewhere [*Rodger et al.*, 2014], and are being considered for a future detailed publication.
507 Here we restrict ourselves to reporting on some issues in the AIMOS-ionization rates which
508 were identified in the initial data quality checks. We made use of AIMOS v1.2 which has
509 been extensively used to describe the particle forcing during solar proton events and
510 geomagnetic storms [e.g., *Funke et al.*, 2011], and has been validated for thermospheric
511 altitudes [*Wissing et al.*, 2011], but not below. AIMOS provides ionization rate profiles for a

512 given location and time range, with separate rates produced caused by the precipitation of
513 protons, electrons and alpha particles.

514 Initial data quality checks identified numerous issues with the ionization rates from AIMOS
515 v1.2 indicating great care must be taken when drawing conclusions from studies using these
516 models. We provide a summary of areas of concern below:

517 1.) It has long been recognized that the MEPED/POES electron detectors suffer over-
518 whelming contamination during solar proton events [*Evans and Greer, 2004*]. However,
519 AIMOS v1.2 clearly includes these electron observations during solar proton events, leading
520 to highly unrealistic electron ionization rates inconsistent with experimental observations
521 [e.g., *Funke et al., 2011*]. The upper panel of Figure 9 shows the electron precipitation-
522 produced ionisation rates for 3 months in 2006-2007 for the path from NAA to SGO. Here the
523 blue line over-plotted on the ionisation rates represents the GOES-reported >10 MeV proton
524 flux (ranging from $\sim 0.2 \text{ cm}^{-2}\text{s}^{-1}\text{sr}^{-1}$ to $1.95 \times 10^3 \text{ cm}^{-2}\text{s}^{-1}\text{sr}^{-1}$); a solar proton event occurred
525 beginning on 5 December 2006. The over-plotted lower black line shows the variation in the
526 geomagnetic index Kp (which ranges from 0 to 8.3). During the December 2006 solar proton
527 event the ionization rates for proton precipitation-produced ionization (from 50-90 km
528 altitudes) increase by 4-5 orders of magnitude (not shown). At the same time the ionization
529 rates reported by AIMOS due to electrons also increase by $\sim 4-5$ orders of magnitude, as
530 shown in the upper panel of Figure 9. There is no evidence for this electron precipitation
531 outside of the contaminated POES observations.

532 It is also well known that the MEPED/POES electron detectors suffer contamination from
533 protons of ~ 100 keV at high latitudes [*Evans and Greer, 2004; Yando et al., 2011*]. *Rodger et*
534 *al. [2010a]* found that as much as $\sim 42\%$ of the 0° telescope >30 keV electron observations
535 from MEPED were contaminated by such protons in the energy range although the situation
536 was less marked for the 90° telescope (3.5%). The existing algorithms to correct for proton
537 contamination have not been applied in AIMOS v1.2.

538 2.) During a data quality test we examined the ionization rates near the geomagnetic equator
539 above Fiji (18.2°S, 178.5°E, $L=1.2$) where one would expect no particle input. During the
540 December 2006 solar proton event a two order of magnitude increase in proton produced
541 ionization rates are reported above ~ 70 km altitude (not shown) by AIMOS, and at the same
542 time AIMOS reports a 2-3 order of magnitude increase in electron produced ionization rates
543 for altitudes as low as ~ 45 km. This is seen in the middle panel of Figure 9 which is otherwise
544 in the same format as the panel above. Solar protons cannot penetrate to these geomagnetic
545 latitudes [Rodger *et al.*, 2006], and are not seen in the MEPED/POES data above Fiji. Such
546 protons are not visible in the data until the satellites are located more than 30° poleward of
547 Fiji, indicating the polar latitude observations are being incorrectly mapped into mid- and
548 low-latitudes. Serious issues exist around the latitudinal binning of the satellite data to
549 produce the precipitation input.

550 3.) The lower panel of Figure 9 shows the variation in AIMOS v1.2-reported EEP-produced
551 ionization rates for the path from NAA to SGO for 4 months in late 2006 and a selection of
552 mesospheric altitude ranges. This time range was selected to ensure no solar proton event
553 occurred. The ionization rates are normalized and shifted along the y-axis to provide easy
554 comparison. Here the black line shows the variation in the geomagnetic index K_p (which
555 ranges from 0 to 6), and the blue line is the changing flux of MEPED/POES >300 keV
556 precipitating electrons (which ranges from ~ 145 to $\sim 6 \times 10^3$ $\text{cm}^{-2}\text{s}^{-1}\text{sr}^{-1}$). Note that electrons
557 with energies above 300 keV should deposit the majority of their energy below ~ 75 km [e.g.,
558 Turunen *et al.*, 2009]. There is a strong correlation between increases in geomagnetic activity
559 and increases in >300 keV EEP, as expected. However, in the altitude ranges from 50-59 km
560 and 60-69 km there is a clear anti-correlation between the ionisation rates, >300 keV EEP
561 magnitude, and geomagnetic activity, and a correlation between the rates and EEP flux in the
562 70-79 km altitude range. Examination of the upper panel of this figure shows that AIMOS
563 v1.2-reported ionization rates above ~ 80 km increase during geomagnetic disturbances, but

564 the opposite occurs below ~ 75 km. For these lower altitudes the ionization rates move from a
 565 quasi-constant value of $\sim 10^7$ - 10^8 to $\sim 10^5$ - 10^6 el. m^{-3} during storms, i.e., a significant decrease
 566 in the ionization rates rather than an increase as expected from the experimental observations
 567 shown in Figure 7 and 8 and indeed in the relevant POES-data itself shown in Figure 9c. We
 568 speculate that this is due to incorrect fitting of the EEP energy spectra in the AIMOS model.

569 4.) As noted above (section 5.1) the MEPED/POES data are comparatively insensitive, with a
 570 noise floor at a rather high flux value ($\sim 10^2$ el. $\text{cm}^{-2} \text{ s}^{-1} \text{ sr}^{-1}$). The AIMOS v1.2 model includes
 571 the MEPED/POES noise-floor data as if they are real precipitating electrons, leading to the
 572 large quiet time mesospheric ionization rates seen in the upper panel of Figure 9. This panel
 573 indicates quiet time rates outside of the SPE period of $\sim 10^6$ - 10^7 el. $\text{m}^{-3} \text{ s}^{-1}$ at ~ 50 - 75 km
 574 altitude. In contrast, the background ionization rates in this altitude range are expected to be
 575 dominated by the effect of Lyman- α and galactic cosmic rays with rate values of $\sim 10^5$ - 10^6 el.
 576 $\text{m}^{-3} \text{ s}^{-1}$ [e.g., *Friedrich et al.*, Fig. 1, 1998; *Rodger et al.*, Fig. 3 & 4, 2007b]. Fluxes at the
 577 MEPED/POES noise floor level are sufficiently high to produce a ~ 4 time increase in the
 578 noontime electron number density at ~ 75 km altitude (not shown).

579 There are clearly numerous serious data quality problems in the AIMOS model outputs at
 580 altitudes of 60-80 km. Some of these appear to be due to contamination issues in the input
 581 data (e.g., MEPED/POES proton contamination), others are clearly inherent to the model. The
 582 validity of modeling studies making use of AIMOS v1.2 is questionable, and great care must
 583 be taken when considering the conclusions of such studies. To summarize, the AIMOS v1.2
 584 ionization rates are unlikely to be accurate in the mesosphere and upper stratosphere during:
 585 geomagnetically quiet times (when EEP levels are low), for mid- and low- latitudes, during
 586 solar proton events, or during geomagnetic storms (when there are high levels of EEP).

587 **7. Discussion**

588 **7.1 Comparison with *Clilverd et al.* [2010]**

589 Our study has introduced a number of improvements to the analysis and modeling relative to
590 the original *Clilverd et al.* [2010]. In particular, we have used a more advanced D-region
591 model for calculating the equilibrium electron number density using *Rodger et al.* [2012]
592 rather than *Rodger et al.* [2007a], improved on the data analysis so our QDC is not as
593 simplistic, and allowed for the EEP energy spectra to change. We discuss the significance of
594 each of these in turn.

595 The equilibrium electron number density is calculated from the ionization rate along with
596 attachment and recombination rates. In the *Clilverd et al.* [2010] study these were from
597 *Rodger et al.* [2007a], while we have used those from *Rodger et al.* [2012] which were found
598 to be more broadly representative. This leads to a decrease in the EEP fluxes, with the typical
599 $>30\text{keV}$ EEP flux magnitudes being ~ 0.55 of those reported by *Clilverd et al.* [2010].

600 The data-derived QDC is similar, but not identical to that determined by *Clilverd et al.*
601 [2010], as shown in our Figure 4. Our changing QDC produces both increases and decreases
602 in the EEP magnitude relative to the earlier *Clilverd et al.* [2010] study. On average the
603 typical $>30\text{keV}$ EEP flux magnitudes produced by varying the QDC are ~ 0.51 of those
604 reported by *Clilverd et al.* [2010].

605 The most significant driver for flux magnitude differences between the current study and the
606 earlier *Clilverd et al.* [2010] work comes from allowing the energy spectral gradient of the
607 precipitating fluxes to vary, rather than holding it at a constant value of -2 . During quiet times
608 the energy spectral gradient has values from about -1 to 0 , leading to significant over-
609 estimates of the flux magnitude when a constant -2 gradient value is taken. In contrast for
610 storm times the energy spectral gradient has values from -4 to -2 , and the fixed-case modeling
611 can suggest 1-2 order of magnitude EEP lower magnitudes. On average the typical $>30\text{keV}$
612 EEP flux magnitudes for a fixed $k=-2$ gradient value are ~ 14 times larger than for a varying
613 gradient. Clearly, it is highly important to include the effect of varying energy spectral
614 gradients where possible.

615 **7.2 Application in Chemistry-Climate Models**

616 As noted in the introduction there is growing interest in a broad scientific community into
617 the impact of EEP upon polar atmospheric chemistry, and the potential link to climate. This
618 interest is driving researchers towards incorporating EEP into chemistry-climate models to
619 better represent the polar system, and also to test the overall significance. Due to previous
620 scientific efforts different examples of intense particle precipitation, for example solar proton
621 events, can already be included in chemistry-climate models [e. g., *Jackman et al.*, 2009]. Our
622 current study, along with some of our previous papers, suggests that it is possible to
623 accurately describe EEP using MEPED/POES observations for fairly strong events, assuming
624 sufficient care is taken with the data processing. The question of what to do when
625 MEPED/POES reports fluxes near to the instrumental noise floor remains. Our initial
626 recommendation would be set the EEP magnitude at those times to zero, taking a
627 conservative view. We suggest that sensitivity tests using chemistry-climate models as to the
628 significance of EEP fluxes below this noise floor value should be undertaken to determine
629 whether setting those periods to zero is too harsh a condition or not.

630 We believe that the AARDDVARK-extracted EEP fluxes produced in the current study
631 could be used for an initial test into the significance of EEP in chemistry-climate models, and
632 also to examine the ability of these fluxes to reproduce the observed ozone signatures during
633 EEP events [e.g., *Andersson et al.*, 2014]. However, further work in this area is needed before
634 truly realistic global EEP fluxes can be incorporated into chemistry-climate models. We
635 suggest future focus on longitudinal/MLT variability, and increased energy resolution (and in
636 particular correlations or otherwise between medium and relativistic energy electron
637 precipitation) would be of value in this research area.

638 In addition, a significant requirement from the atmospheric and modeling community is to
639 push the starting time of the model runs further back into time. The MEPED/POES SEM-2
640 we use in the current study start with the beginning of NOAA-15 operations on 1 July 1998,

641 while MEPED/POES SEM-1 observations began with NOAA-5 in November 1978 and end
642 with NOAA-14 in December 2004. However, climate models are regularly run with
643 significantly earlier start dates, suggesting that more focus on proxies for EEP, for example
644 using simple geomagnetic indices, might be required. Finally, if EEP is to be regularly
645 incorporated into climate model runs consideration should be given to the ease of use for the
646 climate modelers. This appears to be one of the strengths of the AIMOS model.

647 **8. Summary and Conclusions**

648 One of the most commonly used sources of EEP measurements are MEPED/POES
649 spacecraft observations. As these spacecraft observations have been made with essentially the
650 same instruments for more than 15 years they have naturally been the focus of researchers
651 wishing to incorporate EEP into various models. They have also been subject to increasing
652 scrutiny due to the growing evidence that EEP leads to significant mesospheric changes in the
653 polar atmosphere which may influence mid- and high-latitude surface climate. However,
654 there are numerous concerns and issues surrounding the MEPED/POES EEP measurements
655 causing uncertainty as to the suitability of their use in such models. We have therefore
656 attempted to make an independent set of long EEP observations by exploiting a ground-based
657 data to compare and contrast with those provided by MEPED/POES.

658 We have analyzed observations of subionospherically propagating VLF radio waves to
659 determine the outer radiation belt EEP flux magnitudes. The AARDDVARK radio wave
660 receivers in Sodankylä, Finland (SGO) have monitored the US Navy transmitter with call sign
661 NAA (Cutler, Maine) near continuously across the time period spanning November 2004
662 until December 2013. Building on an earlier study by *Cilverd et al.* [2010], we have
663 improved upon the dataset, data analysis, and modeling to determine the long time period
664 EEP variations.

665 Our experimental observations include 2859 days worth of good quality NAA-SGO
666 amplitude measurements at one minute resolution. At this point we are limited to EEP
667 extraction for the summer period; the NAA-SGO observations were used to generate 693
668 days worth of EEP flux magnitude values at 1 hour resolutions. These AARDDVARK-based
669 fluxes agree rather well with the essentially independent MEPED/POES precipitation
670 measurements during high intensity precipitation events. Our AARDDVARK observations
671 provide additional confidence that the MEPED/POES precipitation fluxes are reasonable
672 during geomagnetic storms, confirming other recent studies. However, the AARDDVARK
673 EEP observations fall to much lower flux magnitudes than MEPED/POES, indicating that our
674 method of EEP detection is 10-50 times more sensitive to low flux levels than the satellite
675 measurements, largely due to the high noise floor of the MEPED/POES telescopes. Our EEP
676 variations show a good agreement with the variation in lowerband chorus wave powers,
677 providing some confidence that chorus is the primary driver for the outer-belt precipitation
678 we are monitoring.

679 This work continues our efforts to validate EEP fluxes, and to exploit the long
680 AARDDVARK subionospheric observation dataset. At this point our EEP-extraction
681 approaches are limited to summer periods on the NAA-SGO path. We are investigating
682 different analysis and modeling approaches which would allow us to extend to a wide range
683 of ionospheric conditions. This is likely to lead to at least a doubling of the EEP dataset we
684 have generated in the current study.

685 Finally, we presented the result of some initial data quality checks into the outputs of the
686 version 1.2 Atmospheric Ionization Module OSnabrück (AIMOS) model which purports to
687 provide 3-D time-varying numerical information on atmospheric ionization due to
688 precipitating particles. We showed evidence that there are numerous serious data quality
689 problems in the AIMOS model outputs, some due to contamination issues in the input data ,
690 others inherent to the model. AIMOS v1.2 ionization rates are unlikely to be accurate in the

691 mesosphere and upper stratosphere during: geomagnetically quiet times, for mid- and low-
692 latitudes, during solar proton events, or during geomagnetic storms. The validity of
693 modeling studies making use of AIMOS v1.2 is questionable, and great care must be taken
694 when considering the conclusions of such studies.

695

696 **Acknowledgments.** The authors would like to thank the researchers and engineers of
697 NOAA's Space Environment Center for the provision of the data and the operation of the
698 SEM-2 instrument carried onboard these spacecraft. JJN was supported by the University of
699 Otago via a Research Master's Scholarship and a Postgraduate Publishing Bursary. CJR and
700 JJN (partly) were supported by the New Zealand Marsden Fund. MAC was supported by
701 the Natural Environmental Research Council grant NE/J008125/1. Data availability is
702 described at the following websites:
703 http://www.physics.otago.ac.nz/space/AARDDVARK_homepage.htm (AARDDVARK)
704 <http://satdat.ngdc.noaa.gov/sem/poes/data/> (POES SEM-2), and <http://aimos.physik.uos.de/>
705 (AIMOS).

706 **References**

- 707 Andersson, M. E., P. T. Verronen, S. Wang, C. J. Rodger, M. A. Clilverd, and B. R. Carson
 708 (2012), Precipitating radiation belt electrons and enhancements of mesospheric hydroxyl
 709 during 2004–2009, *J. Geophys. Res.*, 117, D09304, doi:10.1029/2011JD017246.
- 710 Andersson, M. E., Verronen, P. T., Rodger, C. J., Clilverd, M. A., and Wang, S.:
 711 Longitudinal hotspots in the mesospheric OH variations due to energetic electron
 712 precipitation, *Atmos. Chem. Phys.*, 14, 1095-1105, doi:10.5194/acp-14-1095-2014, 2014.
- 713 Andersson, M., P. T. Verronen, C. J. Rodger, M. A. Clilverd, and A. Seppälä (2014b),
 714 Missing link in the Sun-climate connection: long-term effect of energetic electron
 715 precipitation on mesospheric ozone, *Nature Comm.*, doi: 10.1038/ncomms6197, (in press).
- 716 Baumgaertner, A. J. G., A. Seppälä, P. Joeckel, and M. A. Clilverd (2011), Geomagnetic
 717 activity related NO_x enhancements and polar surface air temperature variability in a
 718 chemistry climate model: Modulation of the NAM index, *Atmos. Chem. Phys.*, 11(9),
 719 4521–4531, doi:10.5194/acp-11-4521-2011.
- 720 Berthelier, J.J., Godefroy, M., Leblanc, F., Malingre, M., Menvielle, M., Lagoutte, D.,
 721 Brochot, J.Y., Colin, F., Elie, F., Legendre, C., Zamora, P., Benoist, D., Chapuis, Y.,
 722 Artru, J. (2006), ICE, The electric field experiment on DEMETER, *Planet. Space Sci.*, 54
 723 (5), Pages 456-471.
- 724 Brasseur, G., and S. Solomon (2005), *Aeronomy of the Middle Atmosphere: Chemistry and*
 725 *Physics of the Stratosphere and Mesosphere*, third ed., D. Reidel Publishing Company,
 726 Dordrecht.
- 727 Clilverd, M. A., C. J. Rodger, N. R. Thomson, J. B. Brundell, T. Ulich, J. Lichtenberger, N.
 728 Cobbett, A. B. Collier, F. W. Menk, A. Seppälä, P. T. Verronen, and E. Turunen, Remote
 729 sensing space weather events: the AARDDVARK network, *Space Weather*, 7, S04001,
 730 doi: doi:10.1029/2008SW000412, 2009.
- 731 Clilverd, M. A., C. J. Rodger, R. J. Gamble, T. Ulich, T. Raita, A. Seppälä, J. C. Green, N. R.
 732 Thomson, J.-A. Sauvaud, and M. Parrot (2010), Ground-based estimates of outer radiation
 733 belt energetic electron precipitation fluxes into the atmosphere, *J. Geophys. Res.*, 115,
 734 A12304, doi:10.1029/2010JA015638.
- 735 Clilverd, M. A., C. J. Rodger, D. Danskin, M. E. Usanova, T. Raita, Th. Ulich, and E. L.
 736 Spanswick (2012), Energetic Particle injection, acceleration, and loss during the
 737 geomagnetic disturbances which upset Galaxy 15, *J. Geophys. Res.*, 117, A12213,
 738 doi:10.1029/2012JA018175.

- 739 Cresswell-Moorcock, K., C. J. Rodger, A. Kero, A. B. Collier, M. A. Clilverd, I. Häggström,
740 and T. Pitkänen (2013), A reexamination of latitudinal limits of substorm-produced
741 energetic electron precipitation, *J. Geophys. Res. Space Physics*, 118, 6694–6705,
742 doi:10.1002/jgra.50598.
- 743 Daae, M., P. Espy, H. Nesse Tyssøy, D. Newnham, J. Stadsnes, and F. Søråas (2012), The
744 effect of energetic electron precipitation on middle mesospheric night-time ozone during
745 and after a moderate geomagnetic storm, *Geophys. Res. Lett.*, 39, L21811,
746 doi:10.1029/2012GL053787.
- 747 Dowden, R. L., S. F. Hardman, C. J. Rodger, and J. B. Brundell (1998), Logarithmic decay
748 and Doppler shift of plasma associated with sprites, *J. Atmos. Sol. Terr. Phys.*, 60, 741 -
749 753, doi:10.1016/S1364-6826(98)00019-4.
- 750 Drevin, G. R., and P. H. Stoker (1990), Riometer quiet day curves determined by the
751 maximum density method, *Radio Sci.*, 25(6), 1159–1166, doi:10.1029/RS025i006p01159.
- 752 Evans, D. S., and M. S. Greer (2004), Polar Orbiting environmental satellite space
753 environment monitor - 2 instrument descriptions and archive data documentation, NOAA
754 technical Memorandum version 1.4, Space Environment Laboratory, Colorado.
- 755 Ferguson, J. A., and F. P. Snyder (1990), Computer programs for assessment of long
756 wavelength radio communications, Tech. Doc. 1773, Natl. Ocean Syst. Cent., San Diego,
757 California.
- 758 Friedrich, M., D. E. Siskind, and K. M. Torkar (1998), Haloe nitric oxide measurements in
759 view of ionospheric data, *J. Atmos. Sol. Phys.*, 60(15), 1445–1457, doi:10.1016/S1364-
760 6826(98)00091-1.
- 761 Funke, B., Baumgaertner, A., Calisto, M., Egorova, T., Jackman, C. H., Kieser, J.,
762 Krivolutsky, A., López-Puertas, M., Marsh, D. R., Reddmann, T., Rozanov, E., Salmi, S.-
763 M., Sinnhuber, M., Stiller, G. P., Verronen, P. T., Versick, S., von Clarmann, T.,
764 Vyushkova, T. Y., Wieters, N., and Wissing, J. M.: Composition changes after the
765 "Halloween" solar proton event: the High Energy Particle Precipitation in the Atmosphere
766 (HEPPA) model versus MIPAS data intercomparison study, *Atmos. Chem. Phys.*, 11,
767 9089-9139, doi:10.5194/acp-11-9089-2011, 2011.
- 768 Goldberg, R. A., C. H. Jackman, J. R. Barcus, and F. Søråas (1984), Nighttime auroral energy
769 deposition in the middle atmosphere, *J. Geophys. Res.*, 89(A7), 5581–5596,
770 doi:10.1029/JA089iA07p05581.

- 771 Hargreaves, J. K., M. J. Birch, and D. S. Evans (2010), On the fine structure of medium
772 energy electron fluxes in the auroral zone and related effects in the ionospheric D-region,
773 *Ann. Geophys.*, 28, 1107-1120, doi:10.5194/angeo-28-1107-2010.
- 774 Heisler, R., and G. L. Hower (1967), Riometer quiet day curves, *J. Geophys. Res.*, 72(21),
775 5485–5490, doi:10.1029/JZ072i021p05485.
- 776 Hendry, A. T., Rodger, C. J., Clilverd, M. A., Thomson, N. R., Morley, S. K. and Raita, T.
777 (2012) Rapid Radiation Belt Losses Occurring During High-Speed Solar Wind Stream–
778 Driven Storms: Importance of Energetic Electron Precipitation, in *Dynamics of the Earth's*
779 *Radiation Belts and Inner Magnetosphere* (eds D. Summers, I. R. Mann, D. N. Baker and
780 M. Schulz), American Geophysical Union, Washington, D. C.. doi:
781 10.1029/2012GM001299
- 782 Horne, R. B., S. A. Glauert, and R. M. Thorne (2003), Resonant diffusion of radiation belt
783 electrons by whistler-mode chorus, *Geophys. Res. Lett.*, 30, 1493,
784 doi:10.1029/2003GL016963, 9.
- 785 Jackman, C. H., D. R. Marsh, F. M. Vitt, R. R. Garcia, C. E. Randall, E. L. Fleming, and S.
786 M. Frith (2009), Long-term middle atmospheric influence of very large solar proton
787 events, *J. Geophys. Res.*, 114, D11304, doi:10.1029/2008JD011415.
- 788 Lam, M. M., R. B. Horne, N. P. Meredith, S. A. Glauert, T. Moffat-Griffin, and J. C. Green
789 (2010), Origin of energetic electron precipitation >30 keV into the atmosphere, *J.*
790 *Geophys. Res.*, 115, A00F08, doi:10.1029/2009JA014619.
- 791 Li, X., and M. Temerin (2001), The electron radiation belt, *Space Sci. Rev.*, 95(1–2), 569–
792 580, doi:10.1023/A:1005221108016.
- 793 Li, B. Ni, R. M. Thorne, J. Bortnik, J. C. Green, C. A. Kletzing, W. S. Kurth, and G. B.
794 Hospodarsky, Constructing the Global Distribution of Chorus Wave Intensity Using
795 Measurements of Electrons by the POES Satellites and Waves by the Van Allen Probes
796 (2013), *Geophys. Res. Lett.*, 40, 4526–4532, doi:10.1002/grl.50920.
- 797 Lorentzen, K. R., J. B. Blake, U. S. Inan, and J. Bortnik (2001), Observations of relativistic
798 electron microbursts in association with VLF chorus, *J. Geophys. Res.*, 106(A4), 6017–
799 6027, doi:10.1029/2000JA003018.
- 800 McRae, W. M., and N. R. Thomson (2000), VLF phase and amplitude: Daytime ionospheric
801 parameters, *J. Atmos. Sol. Terr. Phys.*, 62(7), 609–618.
- 802 Millan, R. M., and R. M. Thorne (2007), Review of radiation belt relativistic electron loss, *J.*
803 *Atmos. Sol. Terr. Phys.*, 69, 362–377, doi:10.1016/j.jastp.2006.06.019.

- 804 Meredith, N. P., R. B. Horne, M. M. Lam, M. H. Denton, J. E. Borovsky, and J. C. Green
805 (2011), Energetic electron precipitation during high-speed solar wind stream driven
806 storms, *J. Geophys. Res.*, 116, A05223, doi:10.1029/2010JA016293.
- 807 Morley, S. K., R. H. W. Friedel, E. L. Spanswick, G. D. Reeves, J. T. Steinberg, J. Koller,
808 T. Cayton, and E. Noveroske (2010), Dropouts of the outer electron radiation belt in
809 response to solar wind stream interfaces: global positioning system observations, *Proc.*
810 *R. Soc. A*, 466(2123), 3329, doi:10.1098/rspa.2010.0078.
- 811 Newnham, D. A., P. J. Espy, M. A. Clilverd, C. J. Rodger, A. Seppälä, D. J. Maxfield, P.
812 Hartogh, K. Holmén, and R. B. Horne (2011), Direct observations of nitric oxide produced
813 by energetic electron precipitation in the Antarctic middle atmosphere, *Geophys. Res.*
814 *Lett.*, 38(20), L20104, doi:10.1029/2011GL049199.
- 815 Ni, B., J. Bortnik, R. M. Thorne, Q. Ma, and L. Chen (2013), Resonant scattering and
816 resultant pitch angle evolution of relativistic electrons by plasmaspheric hiss, *J. Geophys.*
817 *Res. Space Physics*, 118, 7740–7751, doi:10.1002/2013JA019260.
- 818 Ni, B., W. Li, R. M. Thorne, J. Bortnik, J. C. Green, C. A. Kletzing, W. S. Kurth, G. B.
819 Hospodarsky, and M. de Soria-Santacruz Pich (2014), A novel technique to construct the
820 global distribution of whistler mode chorus wave intensity using low-altitude POES
821 electron data, *J. Geophys. Res. Space Physics*, 119, 5685–5699,
822 doi:10.1002/2014JA019935.
- 823 Parrot, M. (2002). The micro-satellite DEMETER. *Journal of Geodynamics*, 33(45):535 -
824 541.
- 825 Picone, J. M., A. E. Hedin, D. P. Drob, and A. C. Aikin, NRLMSISE-00 empirical model of
826 the atmosphere: Statistical comparisons and scientific issues, *J. Geophys. Res.*, 107(A12),
827 1468, doi:10.1029/2002JA009430, 2002.
- 828 Pincon, J.-L., E. Blanc, P.-L. Blelly, M. Parrot, J.-L. Rauch, J.-A. Savaud, E. Seran (2011),
829 TARANIS — Scientific payload and mission strategy, General Assembly and Scientific
830 Symposium 2011 XXXth URSI, doi: 10.1109/URSIGASS.2011.6050938.
- 831 Rees, M. H. (1989), *Physics and chemistry of the upper atmosphere*, Cambridge University
832 Press, Cambridge.
- 833 Reeves, G. D., et al., (2003), Acceleration and loss of relativistic electrons during
834 geomagnetic storms, *Geophys. Res. Lett.*, vol. 30(10), 1529, doi:10.1029/2002GL016513.
- 835 Reeves, G., A. Chan, and C. J. Rodger, *New Directions for Radiation Belt Research*, *Space*
836 *Weather*, 7(7), S07004, doi: 10.1029/2008SW000436, 2009.

- 837 Rodger, C. J., O. A. Molchanov, and N. R. Thomson (1998), Relaxation of transient
838 ionization in the lower ionosphere, *J. Geophys. Res.*, 103(A4), 6969–6975,
839 doi:10.1029/98JA00016.
- 840 Rodger, C. J., M. A. Clilverd, P. T. Verronen, T. Ulich, M. J. Jarvis, and E. Turunen (2006),
841 Dynamic geomagnetic rigidity cutoff variations during a solar proton event, *J. Geophys.*
842 *Res.*, 111, A04222, doi:10.1029/2005JA011395.
- 843 Rodger, C. J., M. A. Clilverd, N. R. Thomson, R. J. Gamble, A. Seppälä, E. Turunen, N. P.
844 Meredith, M. Parrot, J.-A. Sauvaud, and J.-J. Berthelier (2007a), Radiation belt electron
845 precipitation into the atmosphere: Recovery from a geomagnetic storm, *J. Geophys. Res.*,
846 112, A11307, doi:10.1029/2007JA012383.
- 847 Rodger, C. J., C. F. Enell, E. Turunen, M. A. Clilverd, N. R. Thomson, and P. T. Verronen
848 (2007b), Lightning-driven inner radiation belt energy deposition into the atmosphere:
849 Implications for ionisation-levels and neutral chemistry, *Annales Geophys.*, 25, 1745-
850 1757.
- 851 Rodger, C. J., M. A. Clilverd, J. C. Green, and M. M. Lam (2010a), Use of POES SEM-2
852 observations to examine radiation belt dynamics and energetic electron precipitation into
853 the atmosphere, *J. Geophys. Res.*, 115, A04202, doi:10.1029/2008JA014023.
- 854 Rodger, C J, M A Clilverd, A Seppälä, N R Thomson, R J Gamble, M Parrot, J A Sauvaud
855 and Th Ulich (2010b), Radiation belt electron precipitation due to geomagnetic storms:
856 significance to middle atmosphere ozone chemistry, *J. Geophys. Res.*, 115, A11320,
857 doi:10.1029/2010JA015599.
- 858 Rodger, C. J., M. A. Clilverd, A. J. Kavanagh, C. E. J. Watt, P. T. Verronen, and T. Raita
859 (2012), Contrasting the responses of three different ground-based instruments to energetic
860 electron precipitation, *Radio Sci.*, 47, RS2021, doi:10.1029/2011RS004971.
- 861 Rodger, C. J., A. J. Kavanagh, M. A. Clilverd, and S. R. Marple (2013), Comparison between
862 POES energetic electron precipitation observations and riometer absorptions: Implications
863 for determining true precipitation fluxes, *J. Geophys. Res. Space Physics*, 118, 7810–
864 7821, doi:10.1002/2013JA019439.
- 865 Rodger, C. J., M. A. Clilverd, J. M. Wissing, A. J. Kavanagh, T. Raita, and S. Marple (2014),
866 Testing AIMOS ionization rates in the middle atmosphere: Comparison with ground based
867 radio wave observations of the ionosphere, 31st General Assembly of the International
868 Union of Radio Science, Beijing, China.

- 869 Rozanov, E., L. Callis, M. Schlesinger, F. Yang, N. Andronova, and V. Zubov (2005),
870 Atmospheric response to NOy source due to energetic electron precipitation, *Geophys.*
871 *Res. Lett.*, 32, L14811, doi:10.1029/2005GL023041.
- 872 Russell, C. T., J. G. Luhmann, and L. K. Jian (2010), How unprecedented a solar minimum? ,
873 *Rev. Geophys.*, 48, RG2004, doi:10.1029/2009RG000316.
- 874 Saito, S., Y. Miyoshi, and K. Seki (2012), Relativistic electron microbursts associated with
875 whistler chorus rising tone elements: GEMSIS-RBW simulations, *J. Geophys. Res.*, 117,
876 A10206, doi:10.1029/2012JA018020
- 877 Santolík, O., J. Chum, M. Parrot, D. A. Gurnett, J. S. Pickett, and N. Cornilleau-Wehrin
878 (2006), Propagation of whistler mode chorus to low altitudes: Spacecraft observations of
879 structured ELF hiss, *J. Geophys. Res.*, 111, A10208, doi:10.1029/2005JA011462.
- 880 Seppälä, A., P. T. Verronen, V. F. Sofieva, J. Tamminen, E. Kyrölä, C. J. Rodger, and M. A.
881 Clilverd (2006), Destruction of the tertiary ozone maximum during a solar proton event,
882 *Geophys. Res. Lett.*, 33, L07804, doi:10.1029/2005GL025571.
- 883 Seppälä, A., M. A. Clilverd, and C. J. Rodger (2007), NOx enhancements in the middle
884 atmosphere during 2003-2004 polar winter: Relative significance of solar proton events
885 and the aurora as a source, *J. Geophys. Res.*, D23303, doi:10.1029/2006JD008326.
- 886 Seppälä, A., C. E. Randall, M. A. Clilverd, E. Rozanov, and C. J. Rodger (2009),
887 Geomagnetic activity and polar surface level air temperature variability, *J. Geophys. Res.*,
888 114, A10312, doi:10.1029/2008JA014029.
- 889 Seppälä, A., H. Lu, M. A. Clilverd, and C. J. Rodger (2013), Geomagnetic activity signatures
890 in wintertime stratosphere-troposphere temperature, wind, and wave response, *J. Geophys.*
891 *Res.* 118, doi:10.1002/jgrd.50236.
- 892 Simon Wedlund, M., M. A. Clilverd, C. J. Rodger, K. Cresswell-Moorcock, N. Cobbett, P.
893 Breen, D. Danskin, E. Spanswick, and J. V. Rodriguez (2014), A statistical approach to
894 determining energetic outer radiation belt electron precipitation fluxes, *J. Geophys. Res.*
895 *Space Physics*, 119, 3961–3978, doi:10.1002/2013JA019715.
- 896 Tan, L. C., S. F. Fung, and X. Shao (2007), NOAA/POES MEPED data documentation:
897 NOAA-5 to NOAA-14 data reprocessed at GSFC/SPDF, NASA Space Physics Data
898 Facility.
- 899 Thomson, N. R., and M. A. Clilverd, Solar cycle changes in daytime VLF subionospheric
900 attenuation, *J Atmos. Sol.-Terr. Phys.*, doi: 10.1016/S1364-6826(00)00026-2, 62(7), 601-
901 608, 2000.

- 902 Thorne, R. M. (1977), Energetic radiation belt electron precipitation: A natural depletion
903 mechanism for stratospheric ozone, *Science*, 195, 287– 289.
- 904 Thorne, R. M., T. P. O'Brien, Y. Y. Shprits, D. Summers, and R. B. Horne (2005), Timescale
905 for MeV electron microburst loss during geomagnetic storms, *J. Geophys. Res.*, 110,
906 A09202, doi:10.1029/2004JA010882.
- 907 Thorne, R. M. (2010), Radiation belt dynamics: The importance of wave-particle interactions,
908 *Geophys. Res. Lett.*, 37, L22107, doi:10.1029/2010GL044990.
- 909 Tu, W., R. Selesnick, X. Li, and M. Looper (2010), Quantification of the precipitation loss of
910 radiation belt electrons observed by SAMPEX, *J. Geophys. Res.*, 115, A07210,
911 doi:10.1029/2009JA014949.
- 912 Turner, D. L., Morley, S. K., Miyoshi, Y., Ni, B. and Huang, C.-L. (2012) Outer Radiation
913 Belt Flux Dropouts: Current Understanding and Unresolved Questions, in *Dynamics of the
914 Earth's Radiation Belts and Inner Magnetosphere* (eds D. Summers, I. R. Mann, D. N.
915 Baker and M. Schulz), American Geophysical Union, Washington, D. C.. doi:
916 10.1029/2012GM001310.
- 917 Turunen, E., P T Verronen, A Seppälä, C J Rodger, M A Clilverd, J Tamminen, C F Enell
918 and Th Ulich (2009), Impact of different energies of precipitating particles on NO_x
919 generation in the middle and upper atmosphere during geomagnetic storms, *J. Atmos. Sol.
920 Terr. Phys.*, 71, pp. 1176-1189, doi:10.1016/j.jastp.2008.07.005
- 921 Verronen, P. T., C. J. Rodger, M. A. Clilverd, and S. Wang (2011), First evidence of
922 mesospheric hydroxyl response to electron precipitation from the radiation belts, *J.
923 Geophys. Res.*, 116, D07307, doi:10.1029/2010JD014965.
- 924 Wait, J. R., and K. P. Spies, Characteristics of the Earth-ionosphere waveguide for VLF radio
925 waves, NBS Tech. Note 300, Nat. Inst. of Stand. and Technol., Gaithersburg, Md., 1964.
- 926 Whittaker, I. C., R. J. Gamble, C. J. Rodger, M. A. Clilverd, and J.-A. Sauvaud (2013),
927 Determining the spectra of radiation belt electron losses: Fitting DEMETER electron flux
928 observations for typical and storm times, *J. Geophys. Res. Space Physics*, 118, 7611–
929 7623, doi:10.1002/2013JA019228.
- 930 Whittaker, I. C., C. J. Rodger, M. A. Clilverd, and J.-A. Sauvaud (2014), The effects and
931 correction of the geometric factor for the POES/MEPED electron flux instrument using a
932 multisatellite comparison, *J. Geophys. Res. Space Physics*, 119,
933 doi:10.1002/2014JA020021.
- 934 Wissing, J. M., and M.-B. Kallenrode (2009), Atmospheric Ionization Module Osnabrück
935 (AIMOS): A 3-D model to determine atmospheric ionization by energetic charged

936 particles from different populations, *J. Geophys. Res.*, 114, A06104,
937 doi:10.1029/2008JA013884.

938 Wissing, J. M., M.-B. Kallenrode, J. Kieser, H. Schmidt, M. T. Rietveld, A. Strømme, and P.
939 J. Erickson (2011), Atmospheric Ionization Module Osnabrück (AIMOS): 3. Comparison
940 of electron density simulations by AIMOS-HAMMONIA and incoherent scatter radar
941 measurements, *J. Geophys. Res.*, 116, A08305, doi:10.1029/2010JA016300.

942 Yando, K., R. M. Millan, J. C. Green, and D. S. Evans (2011), A Monte Carlo simulation of
943 the NOAA POES Medium Energy Proton and Electron Detector instrument, *J. Geophys.*
944 *Res.*, 116, A10231, doi:10.1029/2011JA016671.

945 Zhima, Z., J. Cao, W. Liu, H. Fu, J. Yang, X. Zhang, and X. Shen (2013), DEMETER
946 observations of high-latitude chorus waves penetrating the plasmasphere during a
947 geomagnetic storm, *Geophys. Res. Lett.*, 40, 5827–5832, doi:10.1002/2013GL058089.

948

949 _____

950 M. A. Clilverd, British Antarctic Survey (NERC), High Cross, Madingley Road,
951 Cambridge CB3 0ET, England, U.K. (e-mail: macl@bas.ac.uk).

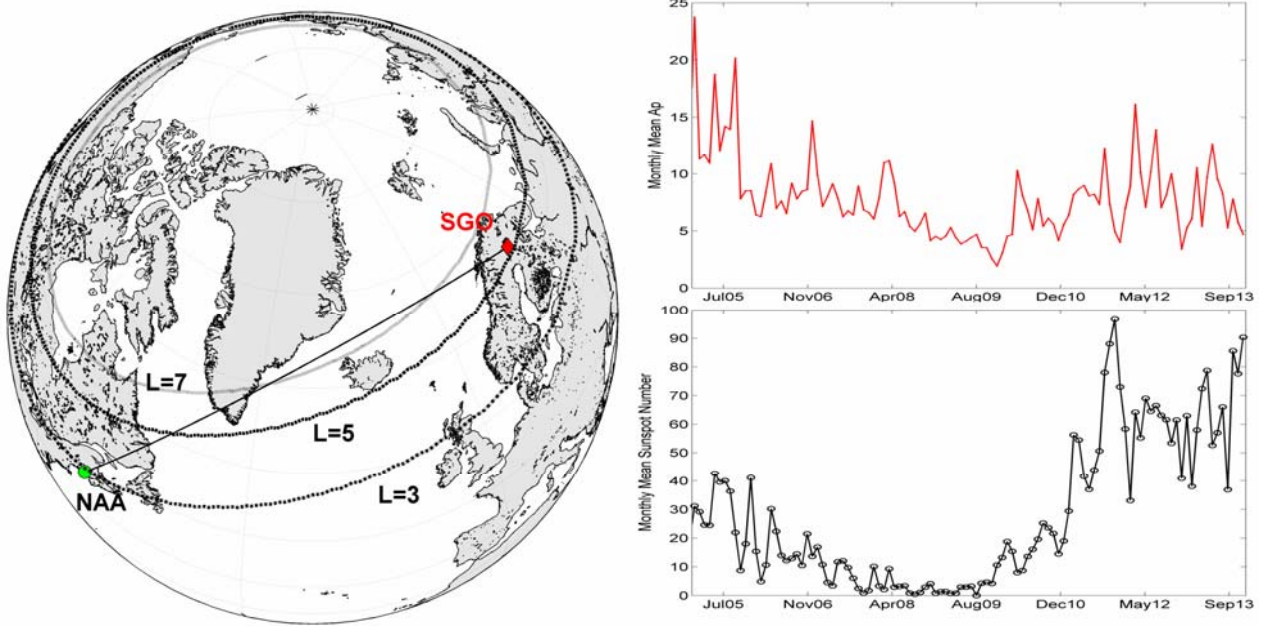
952 J. J. Neal, C. J. Rodger, and N. R. Thomson, Department of Physics, University of Otago,
953 P.O. Box 56, Dunedin, New Zealand. (email: jasonneal13@hotmail.com,
954 crodger@physics.otago.ac.nz, n_thomson@physics.otago.ac.nz).

955 T. Raita, and Th. Ulich, Sodankylä Geophysical Observatory, University of Oulu,
956 Sodankylä, Finland. (email: tero.raita@sgo.fi, thomas.ulich@sgo.fi)

957

958 NEAL ET AL.: LONG TERM EEP FROM AARDDVARK

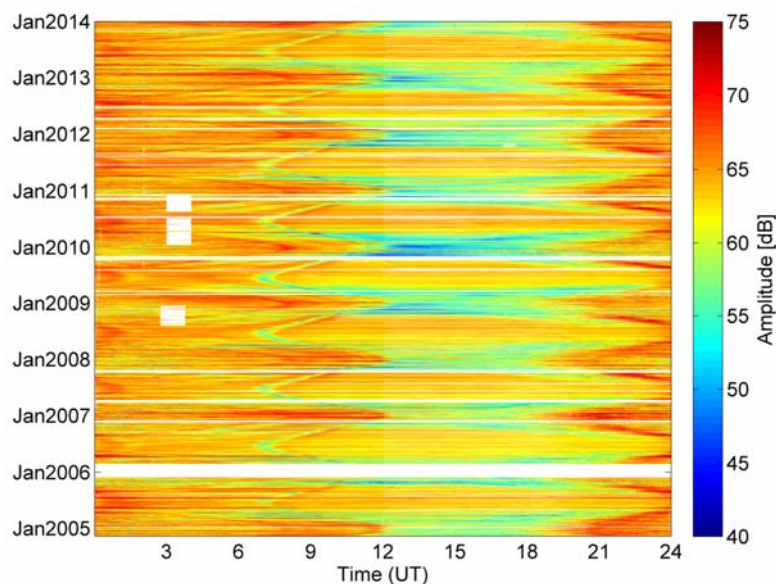
959 **Figures**



960

961 **Figure 1.** Left hand panel) Map of the subionospheric VLF propagation path from the
 962 NAA transmitter to the SGO receiver. Contours of constant L shell are shown indicating the
 963 atmospheric footprints of $L = 3, 5,$ and 7 . Upper right hand panel) Monthly average Ap
 964 value for the period November 2004 to December 2013. Lower right hand panel) Monthly
 965 average sunspot number over the same time period.

966

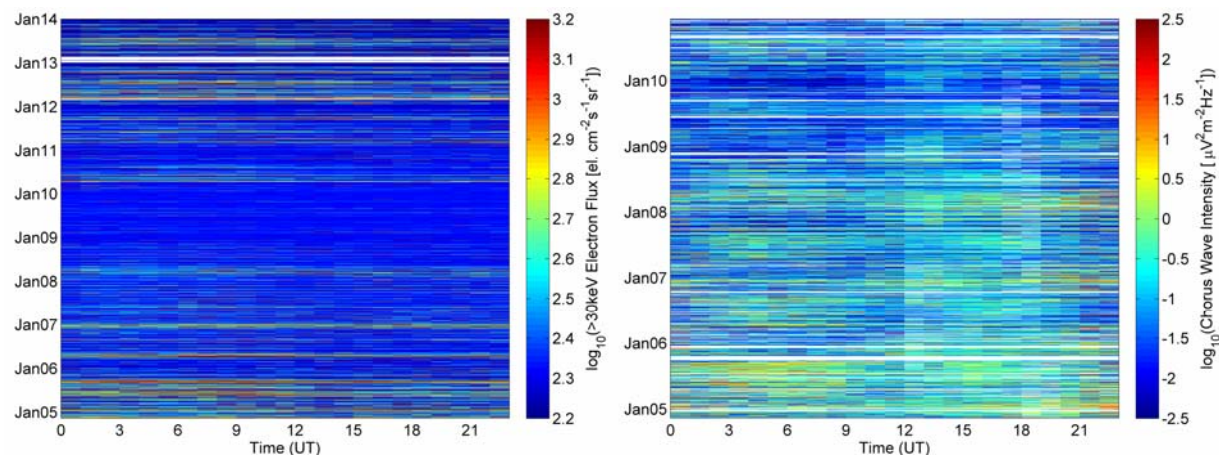


967

968 **Figure 2.** Slightly more than nine years of one minute resolution median amplitudes of the
 969 transmissions from NAA received at Sodankyla (SGO), Finland. The colors represent the
 970 amplitude of the received signal in dB relative to an arbitrary reference level. White regions
 971 correspond to either missing or removed (unreliable) data.

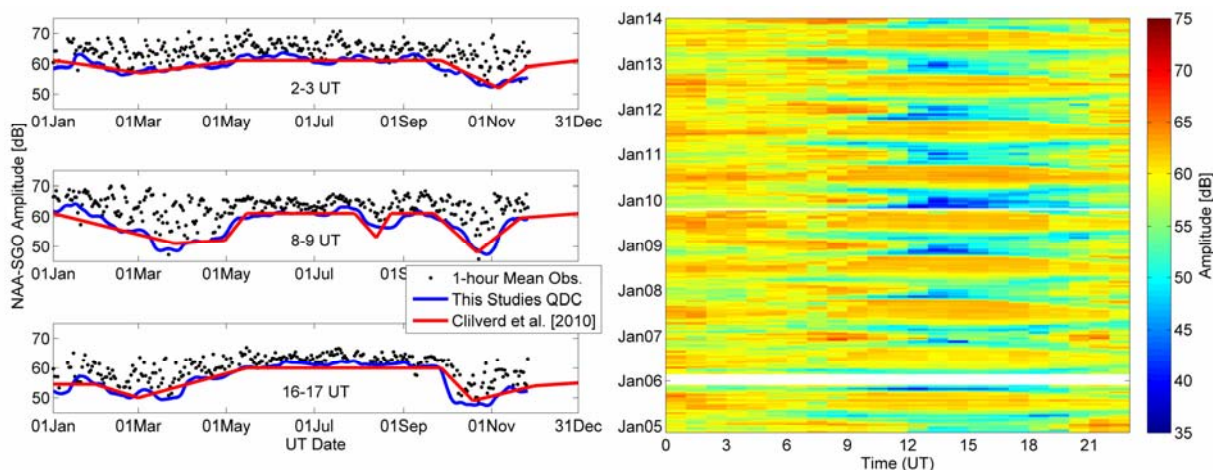
972

973



974

975 **Figure 3.** Left hand panel: Variation in the median hourly POES $0^\circ >30$ keV electron flux
 976 averaged across $L = 3-7$. The 0° electron telescope measures electrons deep inside the BLC.
 977 Right hand panel: Hourly median DEMETER observations of lower-band chorus mode
 978 wave intensity averaged across $L = 3-7$, with no MLT restriction.



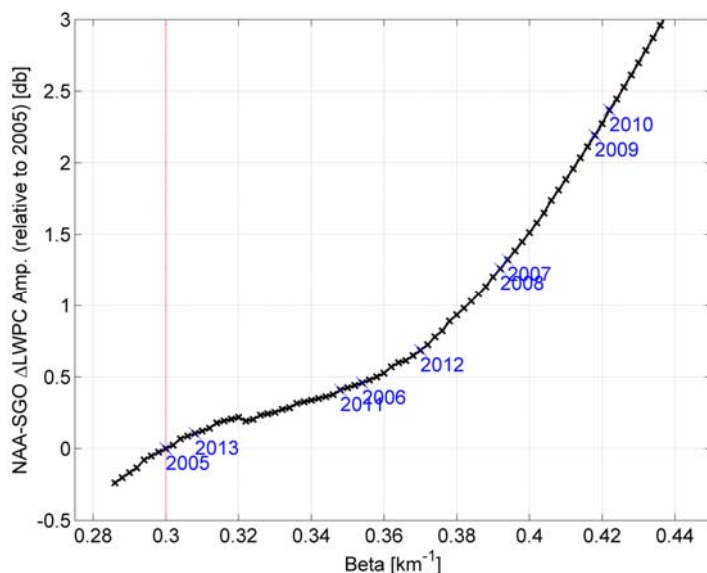
979

980 **Figure 4.** Left hand panel: Examples of QDCs generated in this study (blue) to represent
 981 the 2005 amplitude observations at 2-3, 8-9 and 16-17 UT. The QDCs for the same time
 982 spans presented in *Clilverd et al. (2010)* are shown in red for comparison. The new method
 983 follows the lower edge of the amplitudes more closely, but is similar to that put forward in
 984 the earlier study. Note the large data gap in December 2005, which is also seen in Figure 2.

985 Right hand panel: The QDC generated across our entire ~9 year time period.

986

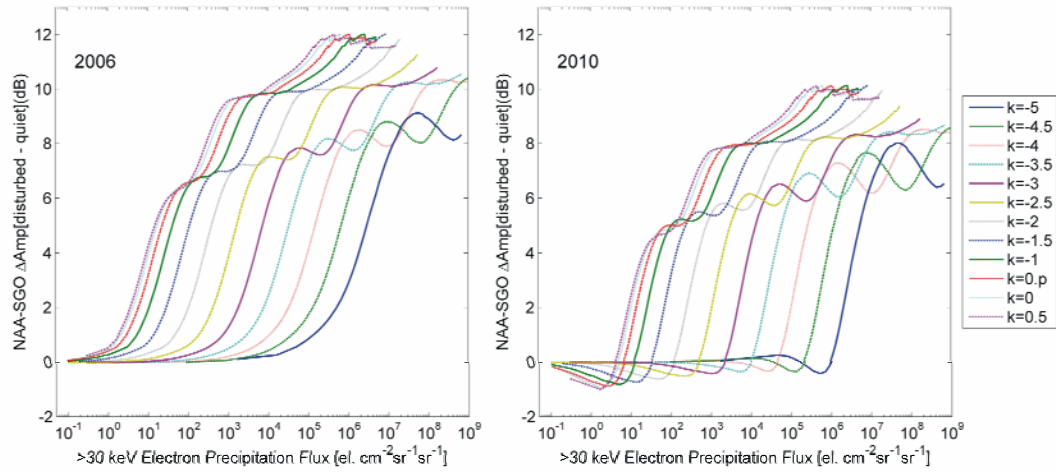
987



988

989 **Figure 5.** Change of the Wait ionosphere β parameter used in the LWPC modeling
 990 determined from the observed QDC noontime amplitude changes across the solar cycle.

991



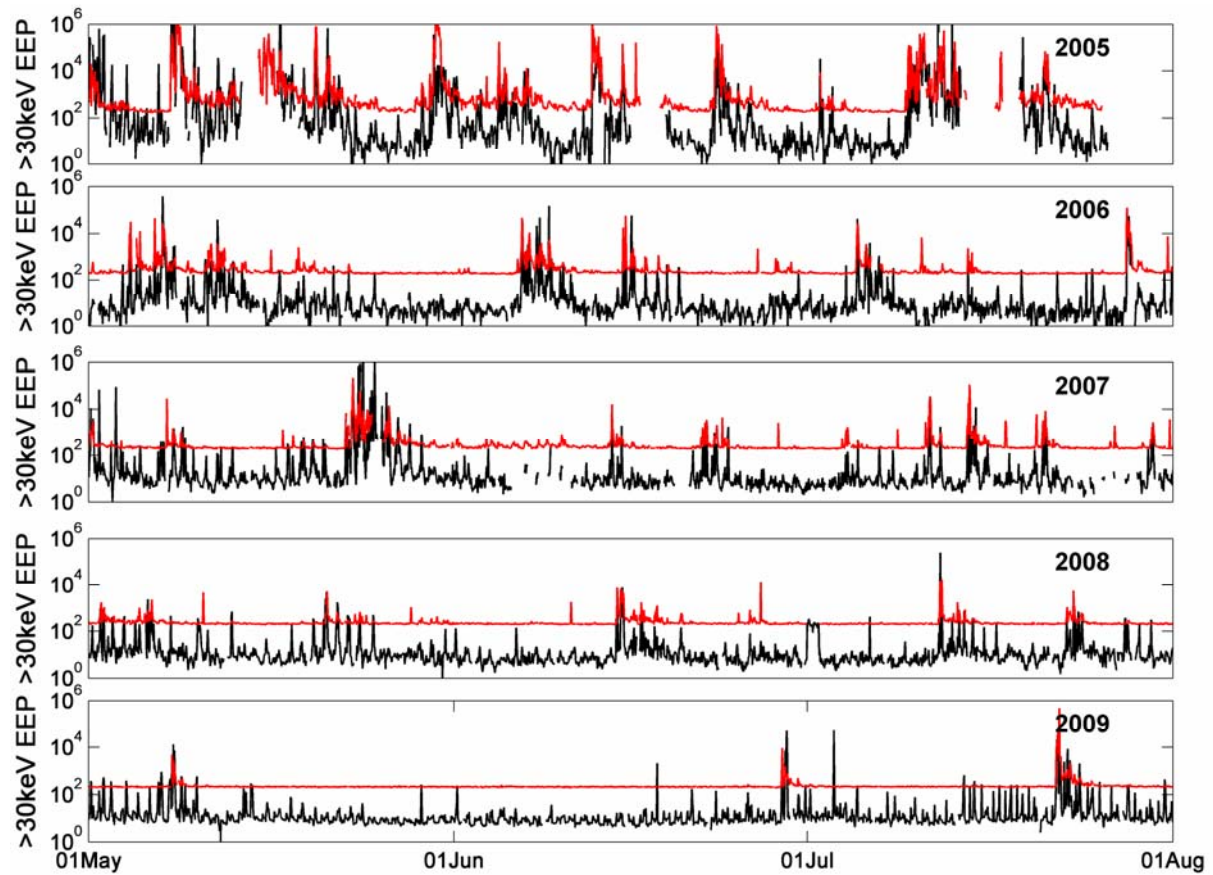
992

993 **Figure 6.** Daytime LWPC modeling of the amplitude changes due to EEP fluxes for the
 994 path NAA-SGO for 2006 (left hand panel) and 2010 (right hand panel). The energy spectra
 995 of the precipitating electrons are specified using a power law which is varied through the *k*
 996 parameter. The modeling used the updated Wait ionosphere parameters for each year shown
 997 in Figure 5.

998

999

1000



1001

1002

1003

Figure 7. Comparison between the NAA-SGO determined EEP flux magnitudes (black)

1004

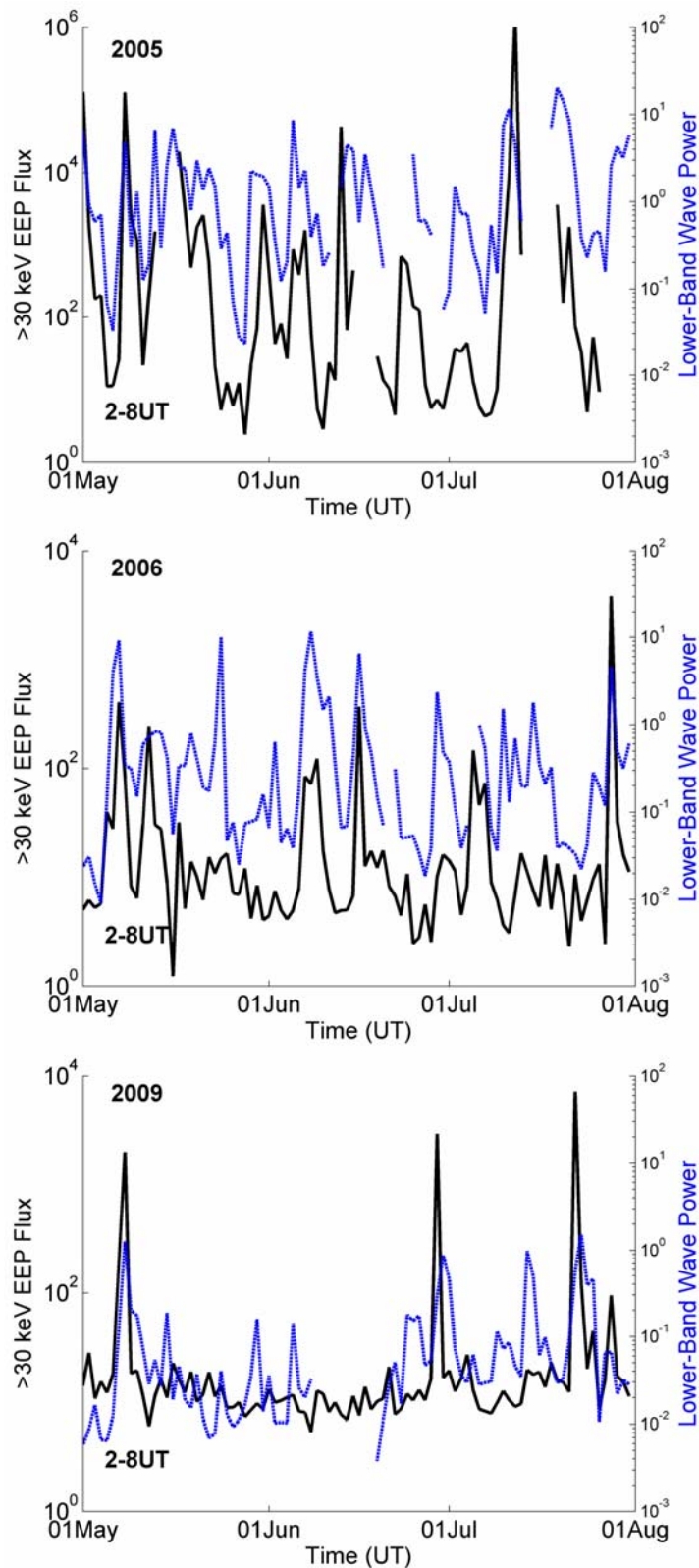
and the MEPED/POES >30 keV electron fluxes (red) during the summer months over 5

1005

years. In all cases the fluxes are shown with units of $\text{cm}^{-2}\text{s}^{-1}\text{sr}^{-1}$. The change in activity level

1006

between solar minimum (~2009) and near solar maximum (2005) can easily be seen.



1007

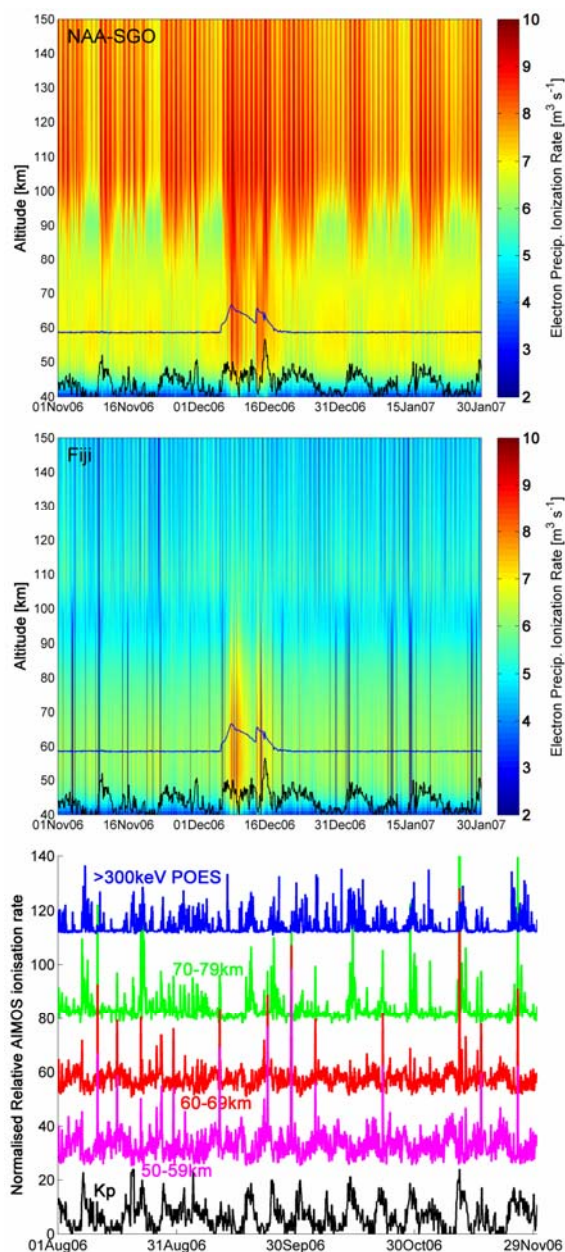
1008

1009

1010

1011

Figure 8. The variation in the NAA-SGO determined EEP flux magnitudes (black line) contrasted with the varying lower-band chorus wave intensity (blue line) observed from the DEMETER satellite. In both cases the median over 2-8 UT is taken for each year.



1012

1013 **Figure 9.** Ionization rates ostensibly due to electron precipitation reported by the AIMOS
 1014 v1.2 model. The upper panel shows the rates for the NAA to SGO path. The black line
 1015 shows the variability in the Kp geomagnetic index, and the blue line the GOES >10 MeV
 1016 proton flux variation. The middle panel shows the ionization rates above Fiji in the same
 1017 format as the panel above. The lower panel shows the normalized variation in the AIMOS
 1018 ionization rates for a range of mesospheric altitudes, with the >300 keV precipitating flux
 1019 from POES EEP variation shown by the blue line and the Kp variation by the black line.
 1020 Note that the lower panel shows a different time-range than the upper two panels.